INL/EXT-20-59819

Light Water Reactor Sustainability Program

Development of RELAP5-3D Modeling of Reactor Core Isolation Cooling (RCIC) System

September 2020

U.S. Department of Energy

Office of Nuclear Energy

INL/EXT-20-59819

Development of RELAP5-3D Modeling of Reactor Core Isolation Cooling (RCIC) System

Hongbin Zhang
Cole Blakley

September 2020

Prepared for the
U.S. Department of Energy
Office of Nuclear Energy

EXECUTIVE SUMMARY

As part of the efforts to understand the unexpected “self-regulating” operation of the RCIC (Reactor Core Isolation Cooling) system that was observed during the Fukushima accidents and to extend boiling water reactor (BWR) RCIC and pressurized water reactor (PWR) TDAFW (Turbine Driven Auxiliary Feed Water) operational range and flexibility, mechanistic models for the Terry turbine were under development. In the previous works, three models - Mach area relations, the isentropic homogenous equilibrium model (IHEM), and the Moody critical flow model – were developed and tested for Terry turbine nozzles using an under-expanded jet model to obtain the velocity and thermodynamic conditions of the Terry turbine stator inlet. The models include both an adiabatic expansion process inside the nozzle and a free expansion process outside of the nozzle to the ambient pressure. The two-phase nozzle expansion model treats the vapor phase with a similar model for the single-phase case with the assumption that the liquid phase would slip along the wall with a much slower speed and will not contribute to the impulse on the rotor. The two-phase Terry turbine nozzle models used the choking models to calculate the mass flow rate, the critical pressure at the nozzle throat, and steam quality.

It was found that the Mach area relations and the IHEM work better under pure vapor conditions at the Terry turbine nozzle inlet. For mixed inlet conditions, the Moody critical flow model provides a means of providing an upper bound for the choked mass flow at the throat, but it is less accurate on predicting phasic velocities at the nozzle exit. With the motivation to develop a fast-running model that can be implemented into a reactor system analysis code like RELAP5-3D and to address the full range of possible two-phase and single-phase inlet conditions at Terry turbine nozzles, a Hybrid Multiphase Discretized Enthalpy Model (HMDEM) is developed in this work. The model development, implementation into RELAP5-3D, verification and partial validation are presented in this report. This effort, in turn, allows the RELAP5-3D code to have the capability to mechanistically model the Terry turbine behavior during the complex, two-phase processes which occur during a station blackout (SBO) accident in a BWR. The validation reveals a strong agreement with the historical Knease nozzle experiment, a data set which had been partially elusive to capture in past modeling efforts. Simulation work has been performed using RELAP5-3D with HMDEM implemented for a generic BWR plant model for a SBO scenario with which both AC and DC power is assumed not available. The simulation results clearly demonstrate the “self-regulating” mode of operation of RCIC during a SBO without any controls. The demonstrated capability of RCIC to operate in a self-regulated mode provides much longer time (coping time) for FLEX to be installed to mitigate a SBO accident. Hence the self-regulation operation of RCIC allows its operation band and flexibility to be expanded and provided enhanced safety margins to the plant. With further validation of the model, HMDEM has the potential to provide the results needed to credit the RCIC self-regulation operations in accident management and mitigation.

CONTENTS

FIGURES

TABLES

ACRONYMS

AC	alternate current
ADS	automatic depressurization system
BDBA	beyond design basis accident
BOC	beginning of cycle
BWR	boiling water reactor
CFD	computational fluid dynamics
CRDHS	control rod drive hydraulic system
CS	core spray
CST	condensate storage tank
DC	direct current
DW	drywell
ECCS	emergency core cooling system
EOC	end of cycle
FLEX	diverse and flexible coping strategies
GE	General Electric
HMDEM	Hybrid Multiphase Discretized Enthalpy Model
HPCI	high pressure core injection
IAPWS	The International Association for the Properties of Water and Steam
IHEM	isentropic homogeneous equilibrium model
MOC	middle of cycle
MSIV	main steam isolation valve
LOCA	loss-of-coolant accident
LPCI	low pressure core injection
PWR	pressurized water reactor
RCIC	reactor core isolation cooling
RELAP5-3D	Reactor Excursion and Leak Analysis Program 5 – 3D
RHR	residual heat removal
RPV	reactor pressure vessel
SBO	station blackout
SLCS	standby liquid control system
SP	suppression pool

SRV	safety relief valve
TBV	turbine bypass valve
TDAFW	rurbine driven auxiliary feedwater
TSV	turbine stop valve
WW	wetwell
ZOFE	zone of flow establishment

Development of RELAP5-3D Modeling of Reactor Core Isolation Cooling (RCIC) System

1. INTRODUCTION

Terry turbines are employed in a wide range of industrial applications such as RCIC systems for boiling water reactors (BWRs) and Turbine Driven Auxiliary Feed Water (TDAFW) systems for pressurized water reactors (PWRs). A Terry turbine [1] is essentially a solid cylindrical wheel with multiple machined semi-circular 'buckets' that are shaped into the body of the wheel. Fixed nozzles and reversing chambers surround the wheel are inside the turbine casing. High pressure steam is accelerated to supersonic flow inside turbine nozzles. The kinetic energy is then converted to shaft work by the impulse force on the turbine buckets.

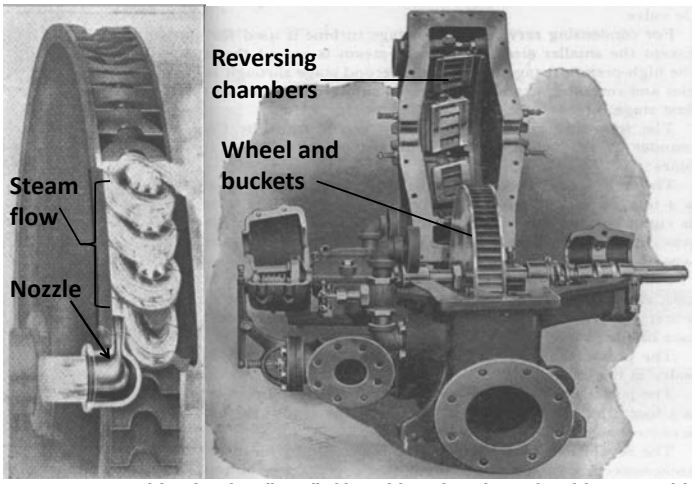

Figure 1-1. Terry turbine bucket flow (left) and interior view of turbine case (right) [1].

The RCIC system, as shown in Figure 1-2 [2], provides makeup water to the reactor pressure vessel (RPV) for core cooling when it is isolated from the secondary plant and the normal water supply to the RPV is lost, and as a standby system for safe shutdown of the plant. Other than a steam-driven Terry turbine, the RCIC system also consists of a turbine-driven pump, piping and valves that are necessary to deliver core makeup water to the RPV at operating conditions. The RCIC turbine is driven by high pressure steam from the main steam lines and the exhaust is discharged to the suppression pool. The RCIC pump supplies makeup coolant to the reactor via the main feedwater lines from the Condensate Storage Tank (CST), or alternatively from the suppression pool once the CST is drained. CST contains a large volume of freshwater that can be used to cool the core. The RCIC system is nearly passive with the exception of requiring battery for control function. The functionality of RCIC is determined by a combination of few factors including the availability of the battery or direct current (DC) power, Heat Capacity Temperature Limits, RPV water level, and RPV pressure. When DC power is available, RCIC water injection is initiated automatically with a low water level signal in the RPV or manually by the plant operator, and it is stopped automatically with a high water level signal in the RPV or manually by the plant operator. The RCIC operates in this way until the vessel pressure and temperature are reduced sufficiently to the point that the Residual Heat Removal (RHR) system can come into operation. The RCIC system is actuated when: (1) station blackout (SBO) occurs and other safety systems are not available, (2) the RPV is isolated from the main turbine and condenser, or (3) feedwater flow is disrupted and high pressure in the RPV prohibits shutdown cooling system action. The RCIC system operates for a wide range of system pressures, from normal operating pressure (~1135 psig) down to 150 psig. When DC power is not available, RCIC can also be blackstarted and blackrun manually by operators. After a normal reactor shutdown, the RCIC turbine is driven by decay heat-generated steam and exhausts to the wetwell. It is noted that RCIC is not considered as part of the ECCS (emergency core cooling system) and does not have a LOCA (loss-of-coolant accident) function,

however it does play an important safety role. LOCA accidents usually depressurize the RPV quickly, thereby disabling the RCIC system.

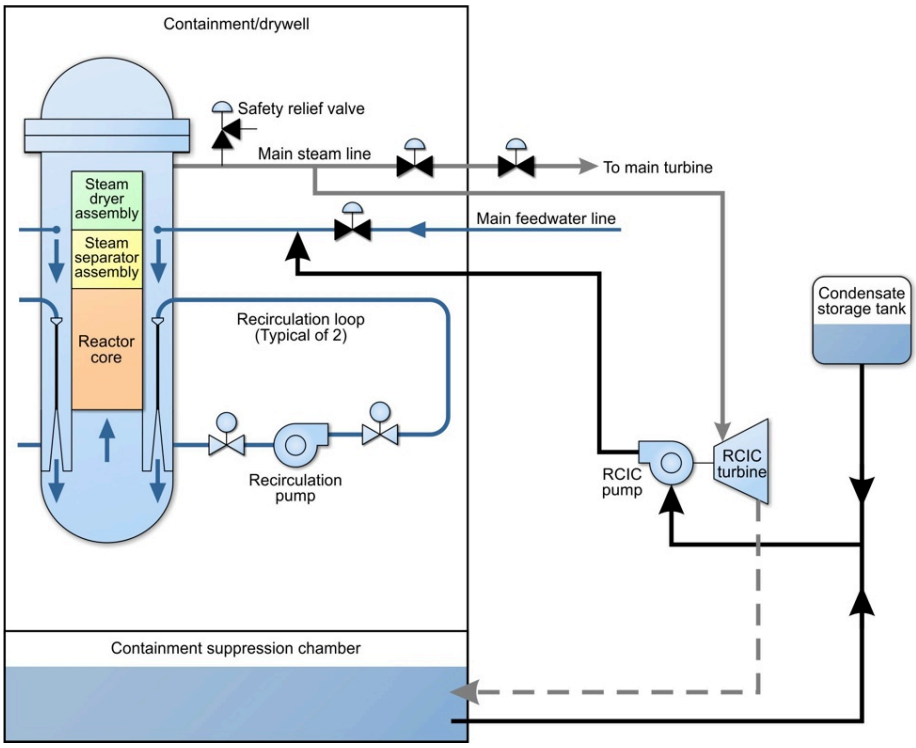

Figure 1-2. Schematic illustration of RCIC system in a BWR [2].

Prior to the Fukushima accidents, all the safety analyses assumed that the RCIC system could not work properly if the Terry turbine inlet is flooded with water. Therefore, battery power (can last from 4 to 12 hours) is required to control the RCIC system in order to prevent the reactor vessel water level from rising too high; otherwise loss of DC power would result in flooding of the steam lines and the subsequent failure of the RCIC system. In contrast, real-world observations from Fukushima Daiichi Unit 2 showed that even with the depletion of battery power and uncontrolled steam line flooding, RCIC system continued to function and provide water injection to the reactor core for nearly three days [3]. As a result, there is a critical need to understand the unexpected “self-regulating” mode of operations of the RCIC system in Fukushima accidents such that BWR RCIC and PWR TDAFW operational range and flexibility can be extended to better mitigate SBO and other accidents. Modeling and simulation can play an important role in this endeavor. However, existing reactor systems analysis codes such as RELAP5-3D [4] do not have mechanistic models to simulate the flow and heat transfer phenomena within Terry turbines, and especially within the nozzles. Previous efforts by Zhao, et. al. [5, 6], and Zhang and Zou [7] on developing modeling capability of RCIC and TDAFW have focused on developing fast-running analytical models for Terry turbine nozzles such that these analytical models can be implemented into systems analysis codes such as RELAP5-3D without negatively affecting their run time. The previous analytical models are developed based on homogeneous and equilibrium assumptions. Three analytical models have been developed in the previous work [5, 6, 7] and they include: (1) classical Mach area relations, (2) the isentropic homogeneous equilibrium model (IHEM), and (3) the Moody critical flow model. An under-expanded jet model was used in the development of those analytical models to obtain the velocity and thermodynamic conditions at the turbine stator inlet. Both an adiabatic expansion process inside the nozzle and a free expansion process outside of the nozzle to ambient pressure were assumed in the model development. For the two-phase off-design conditions, two well-established choking models were used - the IHEM and Moody’s model. The two-phase Terry turbine model used the choking models to calculate the mass flow rate, the critical pressure at the nozzle throat, and steam quality. The two-phase nozzle expansion model was also developed by considering the vapor phase with a similar model for the single-phase case with the assumption that the liquid phase would slip along the wall with a much slower speed and will not contribute to the impulse on the rotor.

For applications within a Terry turbine within a boiling water reactor undergoing station blackout transients, steam nozzles are likely to experience mixed quality inlet conditions and reliable models are needed for mixed quality inlet conditions. Ideally, a model should reasonably approximate inlet flow with quality ranging from zero to unity. However, it was found that the Mach area relations and the IHEM work better under pure vapor conditions at the Terry turbine nozzle inlet. For mixed inlet conditions, the Moody critical flow model provides a means of providing an upper bound for the choked mass flow at the throat, but it is less accurate predicting phasic velocities at the nozzle exit. Lastly, for single-phase liquid inlet conditions, which like the aforementioned models ignore friction, compressible one dimensional inviscid models are common place.

To address the full range of possible inlet qualities, a Hybrid Multiphase Discretized Enthalpy Model (HMDEM) is developed in this work. The focus of this work is to develop, verify, and partially validate the model. HMDEM is compared to existing one dimensional models. The validation reveals a strong agreement with the historical Knease nozzle experiment [8], a data set which had been partially elusive to capture in past modeling efforts [1,9]. A polynomial representation of the HMDEM is performed, allowing for a lower order implementation into RELAP5-3D. This effort, in turn, allows the RELAP5-3D code to have the capability to model the Terry turbine behavior during the complex, multiphase processes which occur during a SBO in a BWR.

The remaining sections of the report are organized in the following manner. Section 2 presents a summary of the models developed in the previous work. Section **Error! Reference source not found.** presents the development of HMDEM. Section 4 presents the implementation, verification, and partial validation of HMDEM. Section 5 provides a demonstration of the “self-regulating” mode of operations for RCIC under SBO accident conditions for a generic BWR model using RELAP5-3D with HMDEM implemented. Section 6 provides conclusions.

2. SUMMARY OF EXISTING TERRY TURBINE NOZZLE MODELS

In order to depict a complete picture of the model development for compressible nozzle flow, this section provides a summary of the three existing models used in the previous work [5, 6, 7]: Mach area relations, the isentropic homogenous equilibrium model (IHEM), and the Moody critical flow model. In the previous work, an under-expanded jet model was used to obtain the velocity for the turbine bucket inlet. The fluid from the turbine nozzle inlet is accelerated to the supersonic condition inside the nozzle and then further expands in the gap between the nozzle exit and turbine bucket inlet. The nozzle models cover both the nozzle internal expansion and free expansion out of the nozzle. Fig. 2-1 shows that the flow through a convergent-divergent nozzle can be characterized with four distinct stages: (1) adiabatic expansion to sonic condition at the throat from the source and adiabatic expansion to supersonic condition in the divergent part of the nozzle, (2) adiabatic free expansion out of the nozzle to ambient pressure (virtual nozzle), (3) zone of flow establishment (ZOFE), (4) free jet. Different models are used for analyzing each stage. The jet is assumed to enter the bucket near the maximum speed, where the jet static pressure is equal to the turbine pressure. Therefore, the zone of flow establishment and free jet models are irrelevant in the simulation and are skipped.

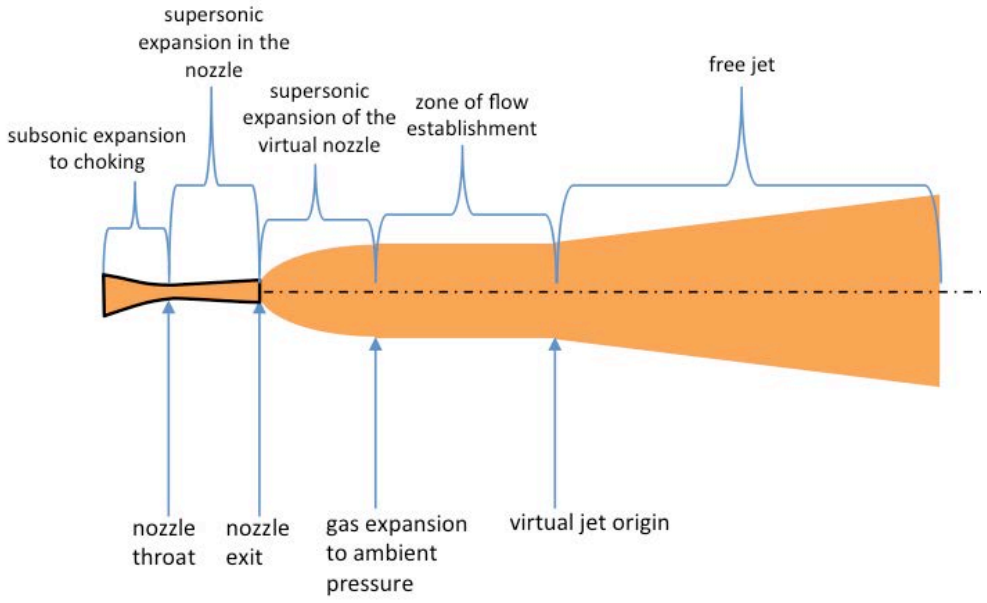

Fig. 2-1. Schematic of high pressure flow through a nozzle.

2.1 Slip Flow with Mach Area Relations

The Mach area relations are ubiquitous within compressible flow literature and are used by Zhao et al. in Ref. [5]. These relations provide a computationally inexpensive means of estimating the velocity and thermodynamic state for a given area ratio and sonic regime (i.e., subsonic or supersonic). Counterintuitively, the area ratio can be expressed as a function of Mach number alone as shown in Eq. 1. Temperature can be obtained from an energy balance assuming a calorically perfect ideal gas (Eq. 2), and pressure can be obtained from isentropic relations for a calorically perfect ideal gas (Eq. 3).

$$A_r{}^2 = \left(\frac{A}{A_t}\right)^2 = \frac{1}{M^2}\left(\frac{2}{\gamma+1}\left(1+\frac{\gamma-1}{2}M^2\right)\right)^{-\frac{\gamma+1}{\gamma-1}} \tag{1}$$

$$T = \frac{T_o}{\left(1+\frac{\gamma-1}{2}M^2\right)^2} \tag{2}$$

$$P = P_o\left(\frac{T}{T_o}\right)^{\frac{\gamma}{\gamma-1}} \tag{3}$$

where A_r is the area ratio, M is the Mach number, γ is the specific heat ratio, P and T are pressure and temperature, and subscript o denotes stagnation conditions. As is the case with ubiquitous formulas, there is a tendency to apply them to situations where the governing mathematical assumptions are not strongly supported. In the case of the Mach area relations, they have at time applied to setting where the gases are not calorically perfect.

Instances of less than ideal application are reacting flow and condensation. In such cases, it is not uncommon to alter the specific heat ratio to account for these complex mechanisms, a method which is not universally supported based off the nonphysical nature of this modification [10]. In reality, in both reacting flows and condensation, the gases behave radically different from calorically perfect gases. Without the calorically perfect assumption, concepts such as the constant specific heat ratio are no longer valid.

2.2 Isentropic Homogeneous Equilibrium Model (IHEM)

The isentropic homogeneous equilibrium model (IHEM) can be applied to any fluid, regardless of whether the fluid is an ideal gas or calorically perfect. As the name implies, isentropic relations are maintained for a homogeneous mixture, meaning no slip between phases. This model is used by Zhao and O'Brein in Ref. [6] and is expressed mathematically in Eqs. 4-6.

$$s = s_o \tag{4}$$

$$h + \frac{1}{2}u^2 = h_o \tag{5}$$

$$\rho(h, s_o)u = G \tag{6}$$

where s is entropy, h is enthalpy, u is velocity, ρ is density, G is mass flux. The mass flux at the throat can be found by maximizing Eqs. 5 and 6 with respect to enthalpy (or an alternative thermodynamic property such as pressure). It is worth noting that by utilizing continuity relations for a uniform velocity, the velocity and thermodynamic state for a given area ratio can be determined via Eq. 7, where subscript t denotes throat conditions.

$$\rho(h, s_o)uA_r = G_t \tag{7}$$

2.3 Moody Critical Flow Model

The Moody critical flow model, also used in Ref. [6], allows for two separate uniform phasic velocities. The ratio between the vapor and liquid phasic velocities is known as the slip factor (K), given in Eq. 8.

$$K = \frac{u_G}{u_L} \tag{8}$$

An isentropic process, wherein the thermodynamic equilibrium is maintained between saturated phases, and total enthalpy and continuity are preserved, is expressed in Eqs. 9-12

$$s = (1-x)s_l + xs_g = s_o \tag{9}$$

$$(1-x)h_l + xh_g + \frac{1-x}{2}{u_l}^2 + \frac{x}{2}{u_g}^2 = h_o \tag{10}$$

$$\alpha\rho_g u_g + (1-\alpha)\rho_l u_l = G \tag{11}$$

$$\alpha = \frac{xv_g/u_g}{xv_g/u_g + (1-x)v_l/u_l} \tag{12}$$

where α is the void fraction and v is the specific volume. Combining Eqs. 8-12 and solving for G yields the Moody critical mass flow relation in Eq. 13.

$$G^2 = \frac{2\left(h_o - h_l(P) - \frac{h_{lg}(P)}{s_{lg}(P)}(s_o - s_l(P))\right)}{\left(\frac{K(s_g(P)-s_o)v_{l,\sigma}(P)}{s_{lg}(P)} + \frac{(s_o - l(P))v_{g,\sigma}(P)}{s_{lg}(P)}\right)^2\left(\frac{s_o - s_{l,\sigma}(P)}{s_{lG}(P)} + \frac{s_{g,\sigma}(P)-s_o}{K^2 s_{lg}(P)}\right)} \tag{13}$$

Eq. 13 states the mass flow as a function of pressure and slip. The maximum mass flow can be found by optimizing with respect to both slip and pressure (Eqs. 14 and 15).

$$\left(\frac{\partial G}{\partial K}\right)_P = 0 \tag{14}$$

$$\left(\frac{\partial G}{\partial P}\right)_K = 0 \tag{15}$$

The optimum slip value can be solved for analytically, and results in Eq. 16

$$K = \left(\frac{v_{g,\sigma}(P)}{v_{L,\sigma}(P)}\right)^{\frac{1}{3}} \tag{16}$$

The optimum pressure value cannot be expressed in a closed form solution and must employ a numerical method such as the golden search ratio. The Moody critical flow method finds the maximum mass flux for an isentropic process which maintains continuity, total enthalpy, and thermodynamic equilibrium. The throat mass flux can conservatively be set to this maximum mass flux value.

However, the Moody critical flow is not typically extended to the diverging section of the nozzle. It is worth noting that the model could be extended to find mass fluxes of diverging section via Eq. 17. Thermodynamic properties and velocities can then be bound by solving Eq. 13 for the mass flux from Eq. 17, while maintaining the optimal slip defined in Eq. 15. All resulting values will be conservative in applications where large mass fluxes are of concern.

$$GA_r = G_t \tag{17}$$

3. HYBRID MULTIPHASE DISCRETIZED ENTHALPY MODEL (HMDEM)

This section presents the development of the HMDEM [11]. The HMDEM is an improvement upon the simplified analytical models of compressible isentropic flow summarized in the previous section as opposed to an addition within the realm of multiphase computational fluid dynamics. This section contains a summary of the model, a description of the outlet boundary conditions, and a brief discussion of the model inaccuracies.

3.1 Derivation of HMDEM

The HMDEM is isentropic and conserves total enthalpy. The model requires a discretization of the enthalpy and it is conceptually illustrated in Figure 3-1. Essentially the model begins with at stagnation conditions, and decreases the enthalpy until exit conditions are reached. For clarity in the nomenclature, the enthalpy and entropy at any area ratio can be expressed as either the value of the mixture (left side of Eq. 18 and 19) or in terms of quality and saturated liquid and gaseous states (right side of Eq. 18 and 19).

$$h = (1 - x)h_l + xh_g \tag{18}$$

$$s = (1 - x)s_l + xs_g \tag{19}$$

The HMDEM iterates through enthalpy according to the simple iterative scheme given in Eq. 20, while maintaining entropy of the mixture (Eq. 21). Subscripts 1 and 2 denote initial and new states for a given iteration.

$$h_2 = h_1 - dh \tag{20}$$

$$s = s_o \tag{21}$$

Since the model assumes homogeneous pressure with saturated liquid and gaseous phases, the thermodynamic information obtained via Eqs. 20 and 21 can be used to obtain all other thermodynamic information from Eqs. 22-26 via the Python based IAPWS library [12]. Note that subscript σ denotes saturation conditions.

$$P_2 = P(h_2, s_2) \tag{22}$$

$$h_{g,2} = h_{g\sigma}(P) \tag{23}$$

$$s_{g,2} = s_{g\sigma}(P) \tag{24}$$

$$h_{l,2} = h_{g\sigma}(P) \tag{25}$$

$$s_{l,2} = s_{g\sigma}(P) \tag{26}$$

The governing equation for liquid velocity is the most difficult to prescribe for a simplified one dimensional model. IHEM assumes equal phasic velocities, while the Moody choked flow selects a slip ratio (Eq. 8) which corresponds to a maximum mass flux.

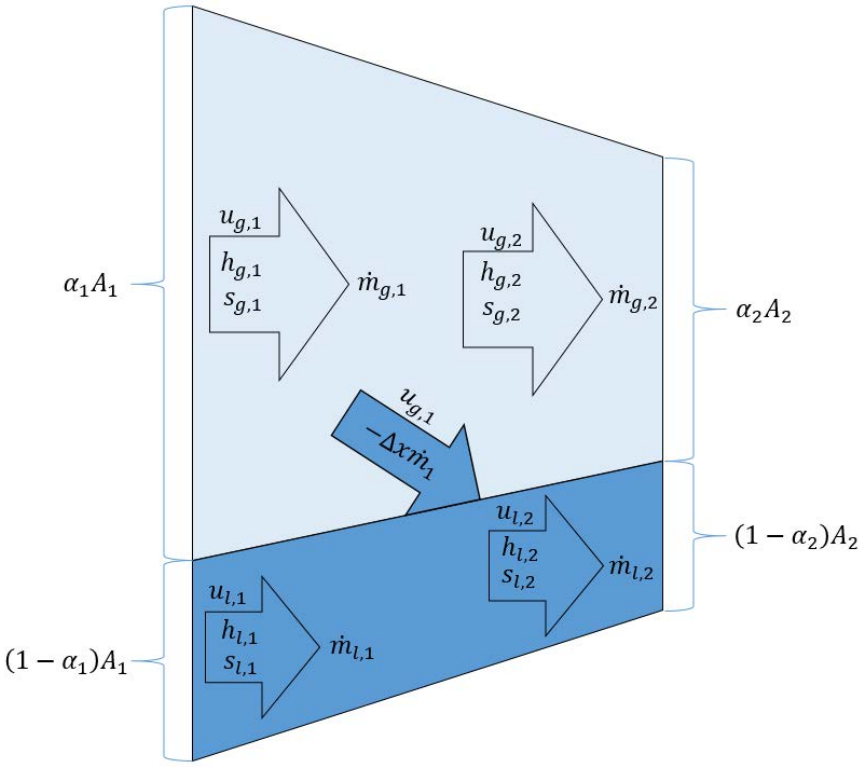

Figure 3-1. Conceptual diagram for HMDEM.

The governing equation for the liquid in this model is a Bernouli like conservation of energy equation given in Eq. 27. The relation accounts for kinetic energy and flow work but ignores liquid internal energy. The internal energy is ignored as the change in temperature that results from following the saturation curve results in nonphysical velocities. In the event of condensation, the Eq. 27 also accounts for momentum transfer from the gaseous to the liquid phase. In order to obtain closed form expressions, the expression for liquid continuity (Eq. 28) is utilized

$$\left(\dot{m}_{l,1} - \Delta x\dot{m}_{g,1}\right)\frac{P_1}{\rho_1} + \dot{m}_{l,1}\frac{1}{2}{u_{l,1}}^2 - \Delta x\dot{m}_{g,1}{u_{g,1}}^2 = \dot{m}_{l,2}\frac{P_2}{\rho_2} + \dot{m}_{l,2}\frac{1}{2}{u_{l,2}}^2 \tag{27}$$

$$\dot{m}_{l,1} - \Delta x\dot{m}_{g,1} = \dot{m}_{l,2} \tag{28}$$

where $\dot{m}_l$ and $\dot{m}_g$ are liquid and gaseous mass fluxes, and Δx is the change in quality between states 1 and 2. By solving for second liquid velocity, Eqs. 27 and 28 are altered into Eq. 29 and 30

$$u_{l,2} = \sqrt{2\left(\frac{P_1}{\rho_{l,1}} - \frac{P_2}{\rho_{l,2}}\right) + \frac{{u_{l,1}}^2 + f{u_{g,1}}^2}{1+f}} \tag{29}$$

$$f = \frac{-\Delta x\dot{m}_{g,1}}{\dot{m}_{l,1}} \tag{30}$$

In the event that quality is sufficiently low, quality will rise as depressurization continues. In this event, momentum transfer from liquid to vapor phase is ignored, resulting in Eq. 31, which is altered into Eq. 32.

$$\frac{P_1}{\rho_1} + \frac{1}{2}{u_{l,1}}^2 = \frac{P_2}{\rho_2} + \frac{1}{2}{u_{l,2}}^2 \tag{31}$$

$$u_{l,2} = \sqrt{2\left(\frac{P_1}{\rho_{l,1}} - \frac{P_2}{\rho_{l,2}}\right) + {u_{l,1}}^2} \tag{32}$$

This relation is selected due to its robustness in dealing with low void fraction inlet conditions. In the event of a single-phase liquid inlet condition, the inviscid solution will take the form of Eq. 32. Thus by incorporating Eq. 32, the full model has the desired asymptotic behavior of approaching the liquid inviscid solution as the void fraction approaches zero.

The gaseous velocity can be obtained from a conservation of energy of the mixture given in Eq. 33, which can be rearranged to Eq. 34.

$$h_1 + \frac{1-x_1}{2}{u_{g,1}}^2 + \frac{x_1}{2}{u_{g,1}}^2 = h_2 + \frac{1-x_2}{2}{u_{g,2}}^2 + \frac{x_2}{2}{u_{g,2}}^2 \tag{33}$$

$$u_{g,2} = \sqrt{\frac{2\cdot(h_1-h_2)+(1-x_1){u_{l,1}}^2+x_1{u_{g,1}}^2-(1-x_2){u_{l,2}}^2}{x_2}} \tag{34}$$

It is worth noting that for the large area ratios of the converging section, Eqs. 29-32 and Eq. 34 can potentially result in slip ratios less than unity, eventually resulting in nonphysical velocities and numerical divergence. To counteract this issue, in the event that $u_{l,2}$ is greater than $u_{g,2}$, a slip ratio of 1 is set, resulting in Eq. 35, effectively using the IHEM model for first initial decreases in enthalpy.

$$u_{l,2} = u_{g,2} = \sqrt{2\cdot(h_1 - h_2) + (1-x_1){u_{l,1}}^2 + x_1{u_{g,1}}^2} \tag{35}$$

The different methods used for liquid versus gaseous velocity is the hybrid aspect of the HMDEM. With the thermodynamic states (Eqs. 23-26) and velocities (Eqs. 29, 32, 34, and 35), the void fraction can be found through continuity relations given in Eq. 12. The liquid and gaseous mass flows are found via Eqs. 36 and 37.

$$\dot{m}_g = \rho_g u_g A\alpha \tag{36}$$

$$\dot{m}_l = \rho_l u_l A(1-\alpha) \tag{37}$$

Rearranging terms in Eq. 36 and Eq. 37 yields expression for the new area for a given iteration (Eq. 38)

$$A_2 = \frac{\dot{m}_{l,1}+\dot{m}_{g,1}}{\rho_g u_g \alpha + \rho_l u_l (1-\alpha)} \tag{38}$$

The expression for area is expressed in terms of mass flow so as to avoid issues with the first iteration, which theoretically begins with an infinite area to create stagnation conditions. The initial mass flow is arbitrarily specified as 1 kg/s, which results in a calculated throat area given in m^2. The resulting calculated mass flow can then be scaled up to the specified throat area of a given problem.

It is also worth noting that quadratic interpolation is used at the throat to obtain the minimum area and all associated velocities and thermodynamic properties. Linear interpolation is used at the outlet boundary conditions in order to more precisely reach a specified area ratio or ambient pressure.

The equations presented in this section provide a fully explicit scheme for calculation of velocities and thermodynamic properties for a given discrete change in enthalpy. Within each iteration of enthalpy decrease,

no coupled calculations requiring internal iterations or implicit matrix operations are required. This results in an efficient algorithm with run times on the order of seconds while executing a single processor.

3.2 Boundary Conditions

All aforementioned models (Mach area relations, IHEM, and Moody critical flow model, and HMDEM) are only valid if a sufficiently large pressure gradient is present to drive the flow to the specified exit area ratio of the diverging section. In the case where the ambient pressure is below the calculated exit pressure, the nozzle is under expanded. For an under-expanded nozzle, a virtual nozzle (as shown in Figure 2-1) forms. The virtual nozzle exit velocity is calculated according to a momentum balance given by Eq. 39.

$$V_{vn,g} = \frac{P_e - P_a + \rho_e u_e{}^2}{\rho_e u_e} \tag{39}$$

In the event the ambient pressure is greater than the calculated exit pressure, the nozzle is over expanded. If the nozzle is grossly over expanded, the flow will separate from the nozzle walls. In order to allow for a simple model which is valid for lower stagnation pressures, all over expanded nozzles are treated as grossly over expanded. This is achieved by stopping the iterative enthalpy stepping process once the ambient pressure is reached. At this point, the flow is assumed to detach and maintain its mass flow, velocity, and thermodynamic state until the geometric exit is reached.

3.3 Model Deficiencies

One of the primary deficiencies of the HMDEM is the neglect of interfacial drag. The inclusion of interfacial drag requires either a wide range of empirical relations, or higher fidelity tools such as dedicated computational codes or neural networks [13]. For the purposes of a lower order model or a steam nozzle, the neglect of interfacial drag is on par with the level of fidelity for one dimensional systems level codes.

HMDEM also assumes that thermodynamic equilibrium is maintained, which prevents the modeling of condensation shocks. The assumption of thermodynamic equilibrium prevents the modeling of subcooled vapor, or superheated liquid, both of which would undoubtedly occur to some extent in certain scenarios. It is also worth noting that HMDEM is fully isentropic, thus skin friction is neglected. Thus this model should not be applied to long piping geometries where frictional effects begin to play more significant roles.

4. HMDEM IMPLEMENTATION, VERIFICATION AND VALIDATION

This section presents the implementation of the HMDEM into the RELAP5-3D code and the verification and validation of the HMDEM.

4.1 HMDEM Implementation into RELAP5-3D

In order to increase the ease of implementation into system level codes, such as RELAP5-3D, a polynomial representation of the HMDEM is presented in this section. The polynomial representation is of lower order, and should only be used for calculations in which lower fidelity is permitted. The systems level code requires the liquid and vapor mass flows entering the steam nozzles. Furthermore, Eqs. 40 and 41 are used to estimate the Terry turbine pump toque,

$$I\frac{d\omega}{dt}+\frac{T_{pump}}{1+\cos\beta}=c_{IC}\left(2r\dot{m}_vV_g\frac{\cos\beta}{1+\cos\beta}-r^2\dot{m}_v\omega\right) \tag{40}$$

$$T_{pump}=c_{IC}\left(2r\dot{m}_vV_g\cos\beta-r^2\dot{m}_v\omega(1+\cos\beta)\right) \tag{41}$$

where I is the moment of inertia, ω is the angular velocity, T_{pump} is pump torque, β is angle between the impinging jet and blades, c_{IC} is the impulse conversion coefficient, r is the turbine radius, $\dot{m}_{g,e}$ is the vapor exit mass flow, and $u_{g,VN}$ is virtual nozzle gas exit velocity. Eqs. 40 and 41 require the virtual nozzle exit velocity and vapor mass flow. Thus four polynomial approximations are needed. The polynomial expansion approximates quantities such as inlet vapor mass flow ($\dot{m}_v$) can be represented as third order polynomials of inlet pressure and void fraction. Eq. 42 shows the polynomial representation of mass vapor flux ($\widehat{\dot{m}_v}$) with $C_{mv,i}$ representing the corresponding polynomial coefficients.

$$\begin{aligned}\widehat{\dot{m}_v}=C_{mv,0}P^3+C_{mv,1}P^2\alpha+C_{mv,2}P\alpha^2+C_{mv,3}\alpha^3+C_{mv,4}P^2+C_{mv,5}P\alpha+\\ C_{mv,6}\alpha^2+C_{mv,7}P+C_{mv,8}\alpha+C_{mv,9}\end{aligned} \tag{42}$$

The polynomial coefficients are found by minimizing the error function given in Eq. 43.

$$E_{RMS}{}^2=\sum_{i=1}^{N}\left(\widehat{\dot{m}_v}(P_i,\alpha_i)-\dot{m}_{v,i}\right)^2 \tag{43}$$

Differentiation of Eq. 43 yields Eq. 44.

$$0=\frac{\partial E_{RMS}}{\partial C_{m,j}}=2\sum_{i=1}^{N}\left(\widehat{\dot{m}_v}(P_i,\alpha_i)-\dot{m}_{v,i}\right)\frac{\partial\widehat{\dot{m}_v}}{\partial C_{m,j}} \tag{44}$$

Rearranging terms of Eq. 44 yields Eq. 45, a linear set of equations which can be expressed in the common matrix format given in Eq. 46.

$$\sum_{i=1}^{N}\widehat{\dot{m}_g}(P_i,\alpha_i)\frac{\partial\widehat{\dot{m}_v}}{\partial C_{m,j}}=\sum_{i=1}^{N}\dot{m}_{g,i}\frac{\partial\widehat{\dot{m}_v}}{\partial C_{m,j}} \tag{45}$$

$$M_{i,j}C_i=B_j \tag{46}$$

A simple matrix inversion operation yields the polynomial coefficients for $\widehat{\dot{m}_v}$. Similar processes are performed to obtain expressions for inlet liquid mass flow ($\widehat{\dot{m}_l}$), inlet liquid mass flow ($\widehat{\dot{m}_l}$), and inlet liquid mass flow ($\widehat{\dot{m}_l}$). The specific parameters for a nozzle used within the specific BWR plant modeled in this work is given in Table 4-1. The sampling parameters used to generate the dataset for the polynomial fit are given in Table 4-2.

Table 4-1. Terry turbine nozzle specifications

Parameter	**Value**
Throat Area	123.15 mm^2
Throat to Exit Area Ratio	1.663
Ambient Pressure	0.101325 MPa

Table 4-2. Sampling parameters for data set for polynomial curve fit

Variable	**Lower Bound**	**Upper Bound**	**Number of Points**	**Distribution**
Inlet Pressure	0.3 MPa	9.3 MPa	10	Uniform
Void Fraction	0.1	1.0	10	Uniform

4.2 Model Verification

The HMDEM is verified by a grid convergence study to confirm that the model is numerically converged and first order accurate. The HMDEM mass flux at the throat is compared to IHEM, Moody critical flow, and a variety of enforced slip factors for both saturated steam and mixed quality inlet conditions. The liquid mass flux is confirmed to follow inviscid single-phase relations for lower void fractions.

4.2.1 Grid Convergence of Enthalpy Discretization

The enthalpy step size is selected so that truncation error is reduced to reasonable and a sensible run time is maintained. A plot of exit velocity versus the inverse of enthalpy time step is given in Figure 4-1. All calculations reported in this work used an enthalpy step of 0.1 J/kg. Figure 4-1 indicates that inaccuracies in exit velocity from truncation error are less than 0.1 m/s, indicating that truncation error is trivial in comparison to input uncertainty and model uncertainty. Figure 4-2 contains a log-log plot of model error from the exit velocity and enthalpy step, indicating the model is first order accurate.

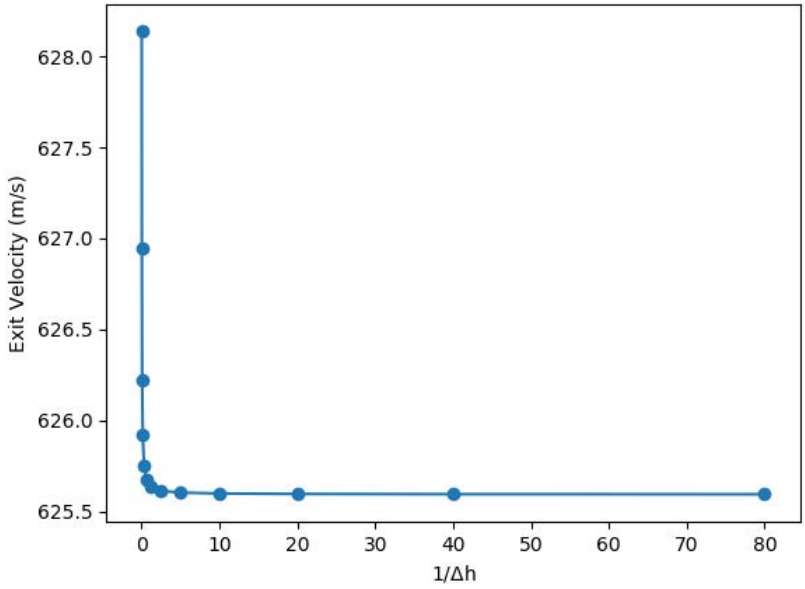

Figure 4-1. Grid convergence study comparing gaseous exit velocity to the inverse of the enthalpy step size

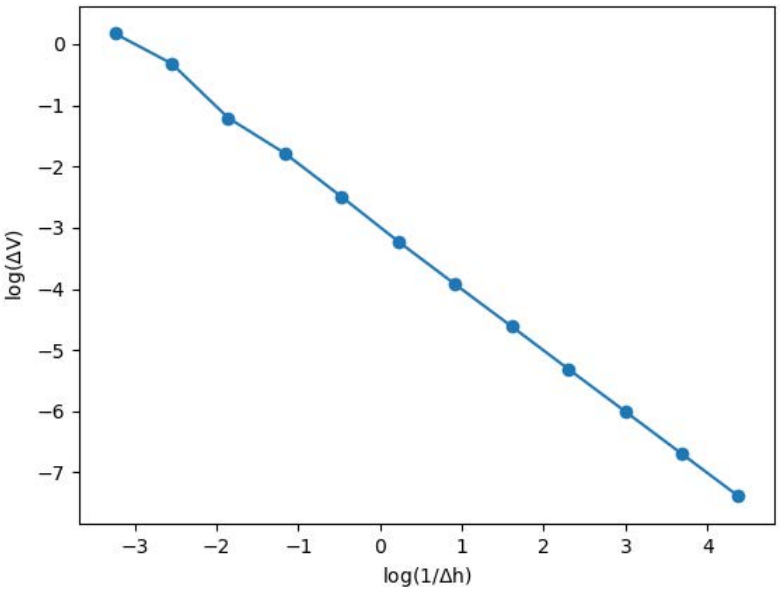

Figure 4-2. Log-log plot of grid convergence study of gaseous exit velocity

4.2.2 Comparison of HMDEM with Mach Area Relations

The true nature of isentropic depressurizations for condensation requires more robust relations, which are employed in both the IHEM, Moody critical flow, and the HMDEM of this work. Figures 4-3 through 4-5 compare HMDEM and the Mach area relations for an arbitrary stagnation inlet condition of 2 MPa. Figure 4-3 contains comparisons for pressure and density, both of which only depart slightly from each other. This is due to

the effects of condensation on mixed quality density being similar to the changes in density of a calorically perfect ideal gas for a given amount of isentropic flow work.

Figure 4-4 shows the short coming of the Mach area relations in dealing with condensation. The Mach area relations predict a nonphysical exit temperatures below 150 K. In reality, the large latent heat of vaporization prevents this extreme lowering of temperatures. Note the deviation in temperature between the two models coincides with the rapid condensation near the throat. The nonphysical temperature of the Mach area relations results in inaccuracies in both the Mach number and the exit velocity shown in Figure 4-5. Thus in applications involving condensation, models which account for latent heat of vaporization are superior to Mach area relations.

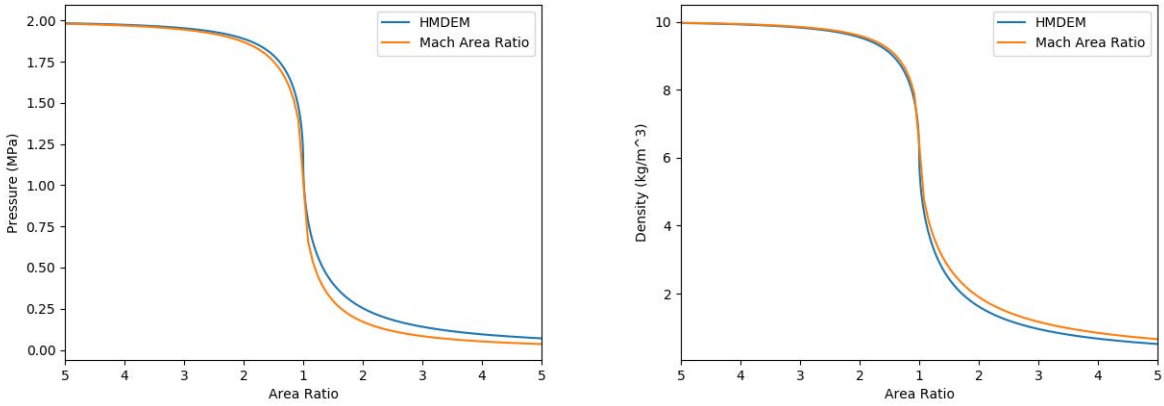

Figure 4-3. Comparison of HMDEM and Mach area relations for pressure and density versus area ratio for 2 MPa stagnation inlet condition

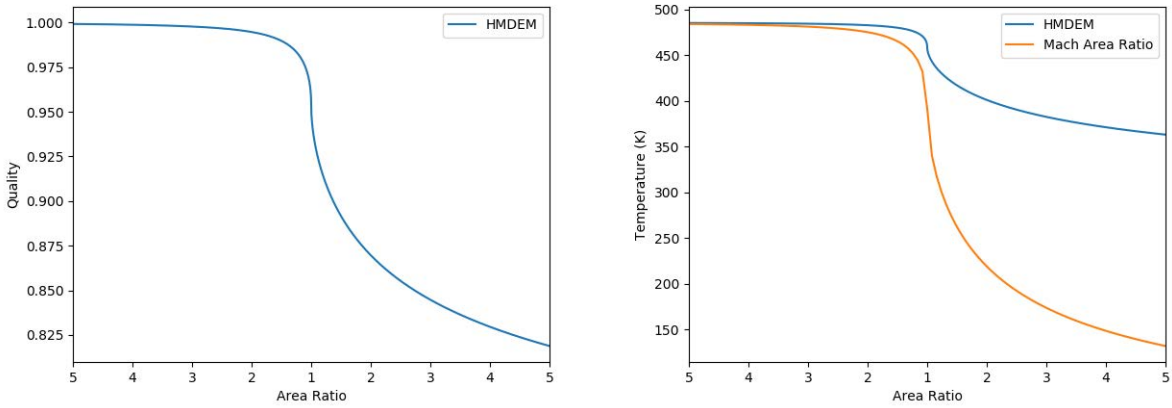

Figure 4-4. Comparison of HMDEM and Mach area relations for temperature and Mach number versus area ratio and quality versus area ratio for HMDEM for 2 MPa stagnation inlet condition

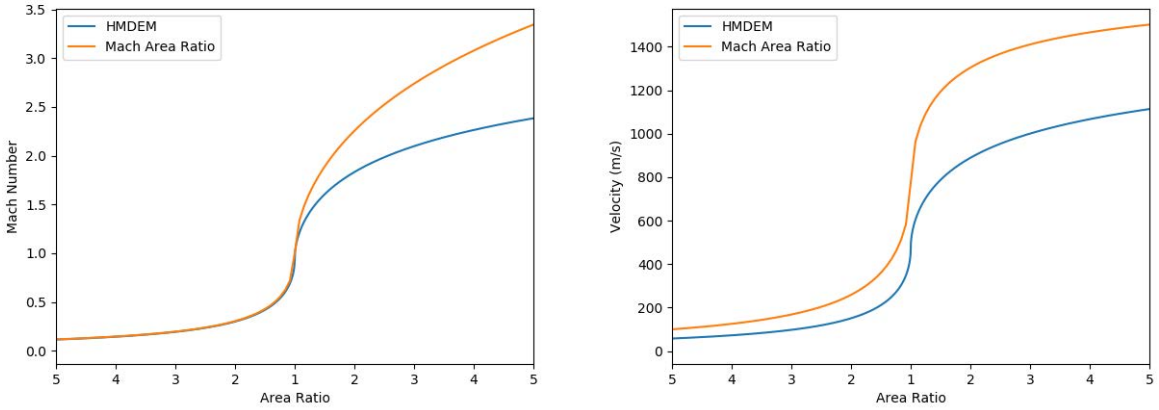

Figure 4-5. Comparison of HMDEM and Mach area relations for velocity versus area ratio for 2 MPa stagnation inlet condition

4.2.3 Pure Steam Comparison of HMDEM

A critical aspect of HMDEM is that it shows strong agreement with existing models for pure steam stagnation inlet conditions. The IHEM, with a variety of slip modifications, as well as the Moody critical flow model, are presented in Figure 4-6. Note that for all the aforementioned models, there is little disagreement in throat mass flux. This is due to the fact that only ~10% of the flow is condensed at the throat, thus both the conservation energy and continuity relations are dominated by the vapor phase, and variations in liquid velocity play a small role.

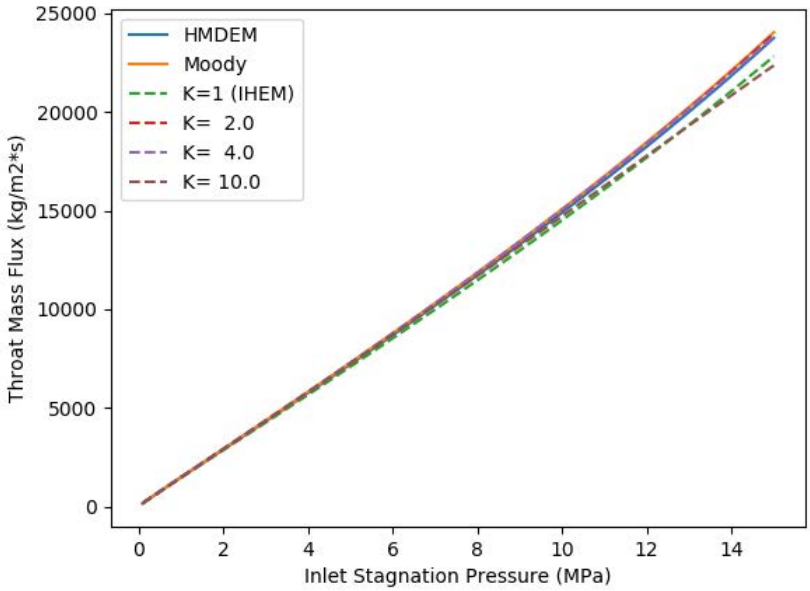

Figure 4-6. Throat mass flux comparison of HMDEM with Moody, IHEM, and specified slip ratio models for saturated steam inlet condition

4.2.4 Mixed Quality Comparison of HMDEM with Moody Critical Flow Model

For mixed quality conditions, the Moody critical flow model provides an upper bound estimate for mass flux within the throat. The Moody model operates by assuming the optimum phasic slip which results in the maximum mass flux. For the sake of comparison with the HMDEM, a variety of slip factor modifications are applied to the Moody critical flow model. These modifications provide a means of quantifying the range of possible mass fluxes resulting from an isentropic process being applied to a stagnant mixed quality fluid assuming that thermodynamic equilibrium is maintained.

Figures 4-7 through 4-10 contain the mass flux versus pressure for fixed slip ratios ranging from 1 to 10, the maximum mass flux for a given pressure (Moody critical flow model value), and the HMDEM values. The inlet void fractions are set to 0.25, 0.5, 0.75, and 0.95 for Figures 4-7, 4-8, 4-9, and 4-10 respectively. Note that the largest discrepancies between the models occur for lower void fractions, where liquid relations are more dominant. For all inlet conditions, HMDEM closely follows, but never exceeds, the Moody critical flow model.

It is worth noting that the Moody critical flow model is a conservative calculation in an application where large mass fluxes are of concern, such as a large break loss-of-coolant accident (LB-LOCA). However, in the case of Terry turbine torque calculation, lower gaseous exit velocities are in fact more conservative. Thus, the slightly lower mass fluxes of the HMDEM model as compared to the Moody critical flow model result in a slightly more conservative calculation.

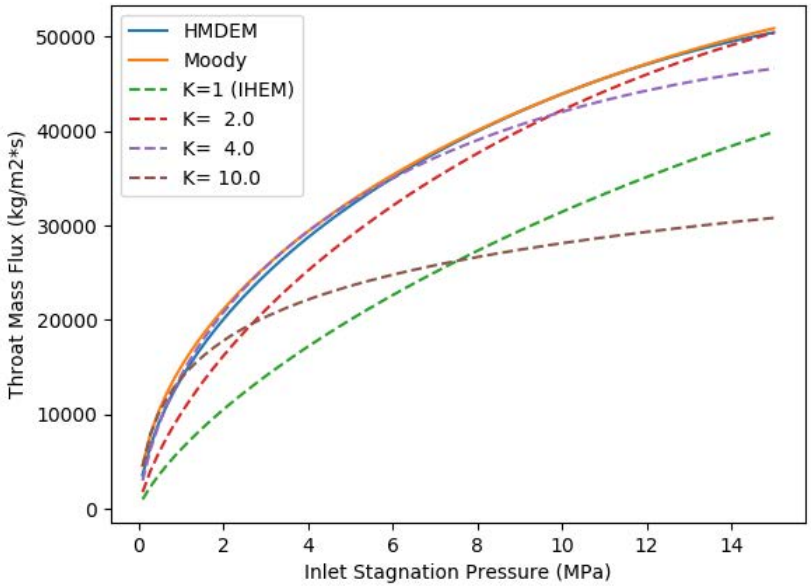

Figure 4-7. Throat mass flux comparison of HMDEM with Moody, IHEM, and specified slip ratio models for inlet void coefficient of 0.25

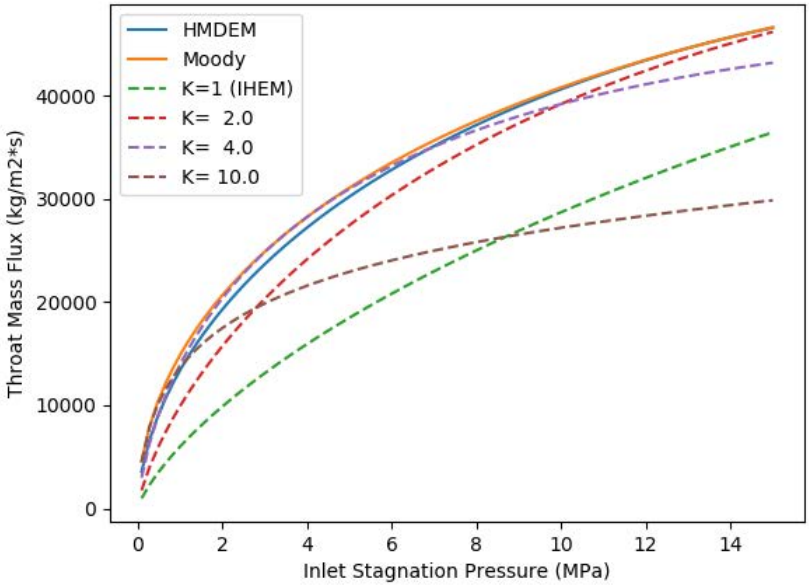

Figure 4-8. Throat mass flux comparison of HMDEM with Moody, IHEM, and specified slip ratio models for inlet void coefficient of 0.5

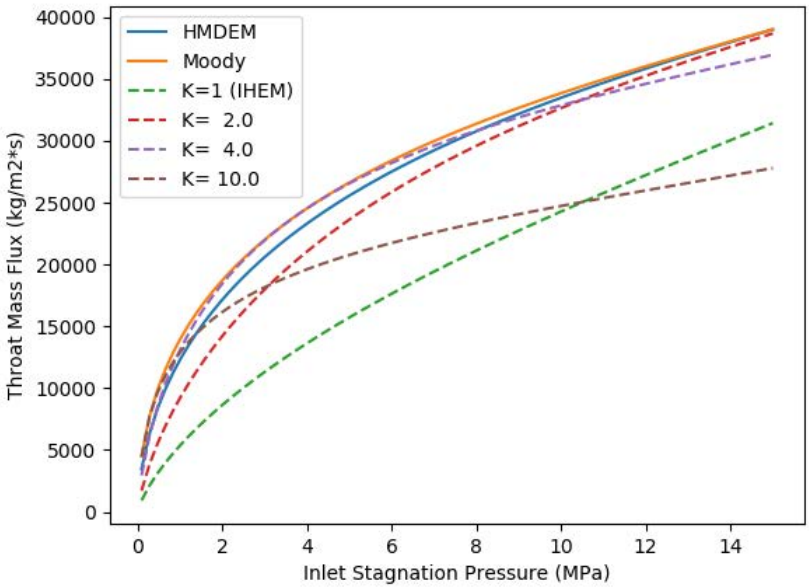

Figure 4-9. Throat mass flux comparison of HMDEM with Moody, IHEM, and specified slip ratio models for inlet void coefficient of 0.75

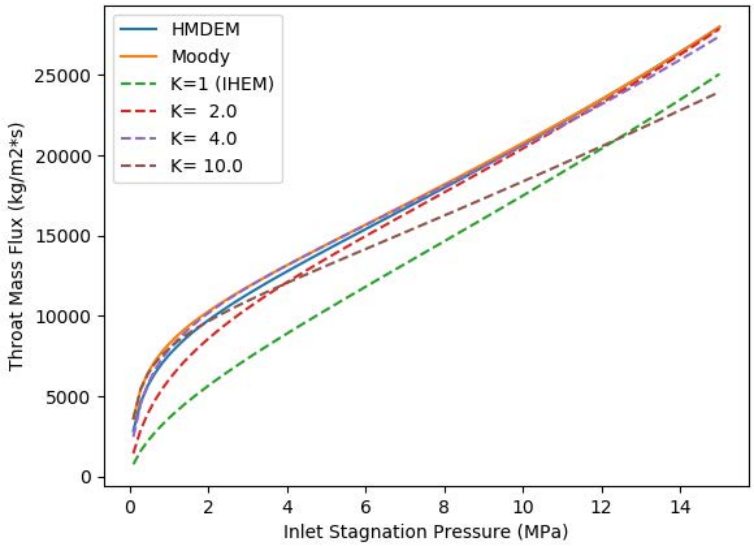

Figure 4-10. Throat mass flux comparison of HMDEM with Moody, IHEM, and specified slip ratio models for inlet void coefficient of 0.95

4.2.5 Pure Liquid Comparison of HMDEM with Inviscid Solution

The incorporation of Eq. 32 within HMDEM results in the liquid mass flux closely following the pure liquid inviscid relations, as shown in Figure 4-11, for void fractions less than ~0.99 for an arbitrary inlet pressure of 2 MPa. The departure from the inviscid relation for higher void fractions is due to kinetic energy transferring from the vapor to liquid phase.

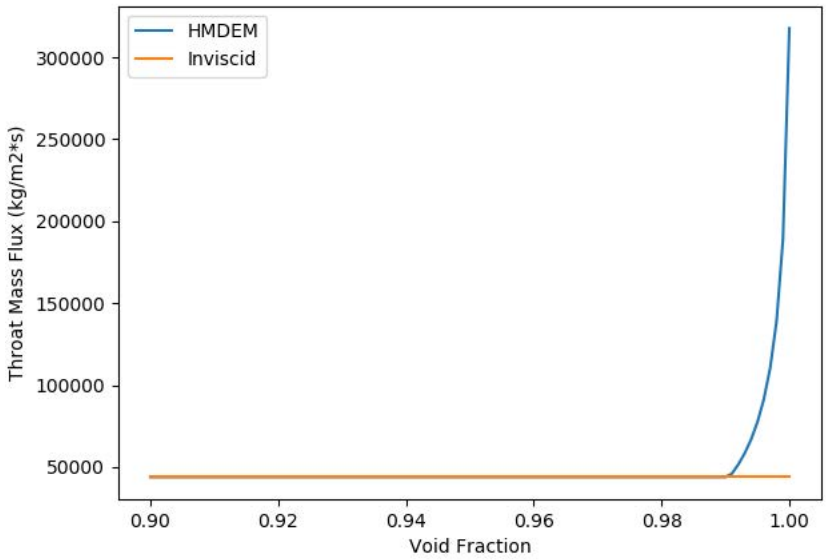

Figure 4-11. Liquid throat mass flux of HMDEM versus liquid mass flux from single-phase liquid inviscid model

4.3 Model Validation

Despite dating back to 1910, the Knease experimental data [8] has been used as a validation in recent studies [1, 5, 9]. Previous work to match the historical data set has had varying degrees of success. The most elusive data point has been the lowest inlet stagnation pressure of 30 psig.

While some have theorized a faulty sensor placement resulting in a poor reading, the work herein presents a different theory. Specifically, given the geometric data available (exit area ratio of 3.005), and the inlet stagnation (30 psig) and ambient atmospheric pressure, it appears the nozzle was grossly over expanded. Thus the flow separation assumptions presented in section 3.1 are likely reasonable. Figure 4-12 and Table 4-3 shows the strong agreement and improvement in modeling resulting from the HMDEM calculations.

Figure 4-12 and Table 4-3 also includes CFD work with FLUENT [1] and a past analytical analysis which incorporated Moody critical flow to throat followed by Mach area relations [5]. The past analytical model captured the relatively flat trend between exit velocity and pressure for saturated steam inlet conditions as compared to calorically perfect gases. This flatter trend is due to the latent heat of vaporization preventing large shifts in thermodynamic properties. However, the past analytical model did not account for the lack of pressure differential present. Without a sufficiently large pressure differential, the flow will not be accelerated to the extreme supersonic conditions dictated by the high exit area ratio of the Knease nozzle. By assuming flow separation, HMDEM appears to capture both the 30 psig data point as well as the trend for 45, 60, and 90 psig. It is worth noting, that HMDEM calculated all of the Knease tests to be over expanded.

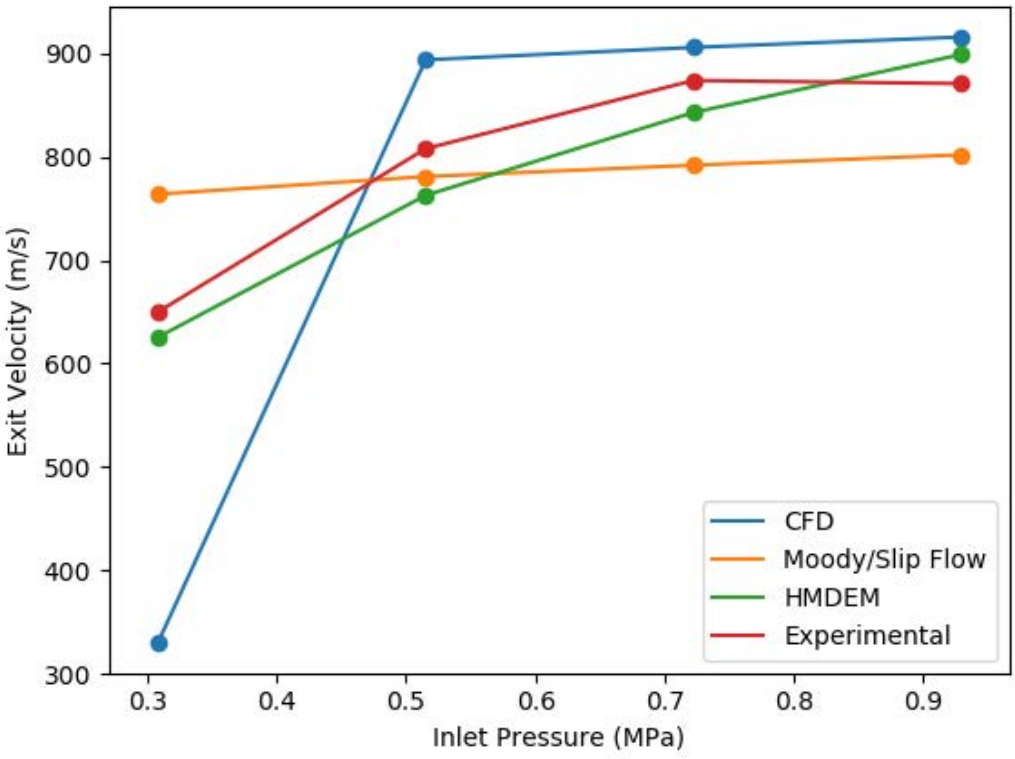

Figure 4-12. Knease nozzle comparison for CFD, Moody/slip flow, HMDEM, and empirical data

The CFD work indicates that at the 30 psig stagnation inlet condition, the flow is unable to maintain quasi-isentropic relations. The lower speed indicates that a strong shock formed in the nozzle, resulting in subsonic velocities. However, it is feasible that the flow in fact separated (as is often the case in grossly over expanded

nozzles), resulting in supersonic velocities which are lower than those governed by area relations alone, but higher than their subsonic velocities resulting from strong shocks.

Table 4-3. Comparison of Knease nozzle data to CFD, Moody/slip flow, and HMDEM predictions.

Inlet Pressure	Nozzle Exit Velocity (m/s)			
	CFD	Moody/Slip Flow	HMDEM	Experimental
30 psig	330	764	626	650
45 psig	894	781	763	808
60 psig	906	792	843	874
75 psig	916	802	899	871

5. DEMONSTRATION OF RCIC "SELF-REGULATING" OPERATIONS UNDER SBO CONDITIONS FOR A GENERIC BWR

This section presents the demonstration of the "self-regulating" mode of RCIC operations under station blackout (SBO) conditions for a BWR using the HMDEM implemented in RELAP5-3D. The plant model is an INL generic BWR model.

5.1 Description of INL Generic BWR Model

The generic RELAP5-3D BWR model used in this study is based on a General Electric (GE) BWR/4 design with Mark I containment, representative of the US BWR fleet. The rated thermal power for this generic BWR is 3293 MWth with 764 fuel assemblies (or bundles) in the core. The reactor pressure vessel (RPV), jet pumps, separator/dryer unit, main steam lines, main feedwater lines, recirculation loops, and safety relief valves (SRVs) are modeled. Figure 5-1 shows the RELAP5-3D nodalization diagram for the generic BWR plant model. The base model can simulate the thermal-hydraulic parameters of the primary side and of some parts of the containment. The major parameters used for the generic BWR model is shown in Table 5-1.

Table 5-1. Major parameters for the generic BWR

Parameters	**Value**
Rated Thermal Power (MWth)	3,293
Number of Fuel Assemblies (Bundles)	764
Core Mass Flow Rate (Kg/s)	11510
RPV Dome Normal Operating Pressure (MPa)	7.02
Feedwater Mass Flow Rate (Kg/s)	1681.3
Recirculation pump flow (Kg/s)	4278.6
Core mass flow rate (Kg/s)	11065.1
Bypass flow (Kg/s)	1266.2
Steam mass flow rate (Kg/s)	1681.3
Feedwater Temperature (^{o}K)	464.394
Feedwater Water Pressure (Mpa)	7.2
RPV Inner Diameter (m)	6.38

The RELAP5-3D model developed for analyzing transient events is based on an input-deck describing:

- RPV
- Main feedwater line
- Main steam line
- Jet pumps
- Recirculation loops

- Reactor core
- Steam separator
- Steam dryer
- Automatic depressurization system (ADS)
- SRVs
- High pressure core injection (HPCI)
- Reactor core isolation cooling (RCIC)
- Core spray (CS)
- Low pressure core injection (LPCI)
- Firehose injection
- Control rod drive hydraulic system (CRDHS)
- Standby liquid control system (SLCS)
- Wetwell
- Drywell
- Vent lines from wetwell to drywell.

The modeling of the RPV includes the downcomer, lower plenum, core, upper plenum, standpipes, separator, dryer, and steam dome. The downcomer is modeled with a series of Annulus component. The steam separator unit is modeled with the simple separator component. The recirculation loops are lumped into one loop and it includes a jet pump, a recirculation pump with pipes from pump suction/discharge. The recirculation pumps and jet pumps allow the operator to vary coolant flow through the core and hence change the power of the nuclear reactor. The jet pump components are located in the region between the core shroud and the vessel wall, submerged in coolant. In order to limit the number of penetrations into the reactor vessel, the recirculation loops also serve as the RHR system. When the reactor is shutdown, the core will continue to generate decay heat, which is removed by bypassing the turbine and dumping the steam directly to the condenser. RHR system provides shutdown cooling when pressure decreases to approximately 0.45 Mpa.

The main feedwater lines are lumped into one. The feedwater systems are modeled using a series of pipe components connected by junctions. The flow rates in the main feedwater line are controlled to maintain the desired downcomer water level in the RPV. High pressure safety systems such as High Pressure Coolant Injection (HPCI) and Reactor Core Isolation (RCIC) will inject coolant through the main feedwater line. Finally, the main steam lines are lumped into one from three original steam lines. The main steam line has one Main Steam Isolation Valve (MSIV), Turbine Bypass Valve (TBV), Turbine Stop Valve (TSV), and turbine modeled with boundary conditions.

The generic BWR model also includes a Mark I containment which consists of a drywell (DW), a wetwell (WW), and vacuum breakers. The WW represents the suppression pool (SP) and the vapor space above it, which jointly form the torus in a typical BWR-4 design. The drywell contains steam or liquid released from SBO, LOCA, etc. and minimizes radioactive leakage.

The WW is essentially a large tank of water which resides within containment of some BWR designs. WW refers to a pressure vessel which contains both a water pool and a non-condensable gas space. The WW water pool is commonly referred to as the SP since excess steam is condensed in this pool in order to suppress possible overpressure events. The SP is also called a suppression chamber or pressure suppression pool. It contains a large volume of freshwater and serves as a heat sink for SRV discharged

steam and exhaust steam from turbines in the high pressure safety systems (i.e., HPCI and RCIC). The WW plays a vital safety role in a SBO and other BWR accident scenarios in that it condenses released high-temperature steam vented from the DW to reduce containment pressure and provides a backup source of water for safety injection systems (the initial default is CST). Steam can vent through the SRVs and the RCIC turbine exhaust into the WW where it condenses. The RCIC pump suction line draws water near the bottom of the WW pool to supply makeup water to the core. The steam injection and condensation taking place in the WW create momentum-induced mixing and buoyancy-induced thermal stratification. These two opposing phenomena determine the thermodynamic conditions of the WW and have a large effect on the overall performance of the RCIC System.

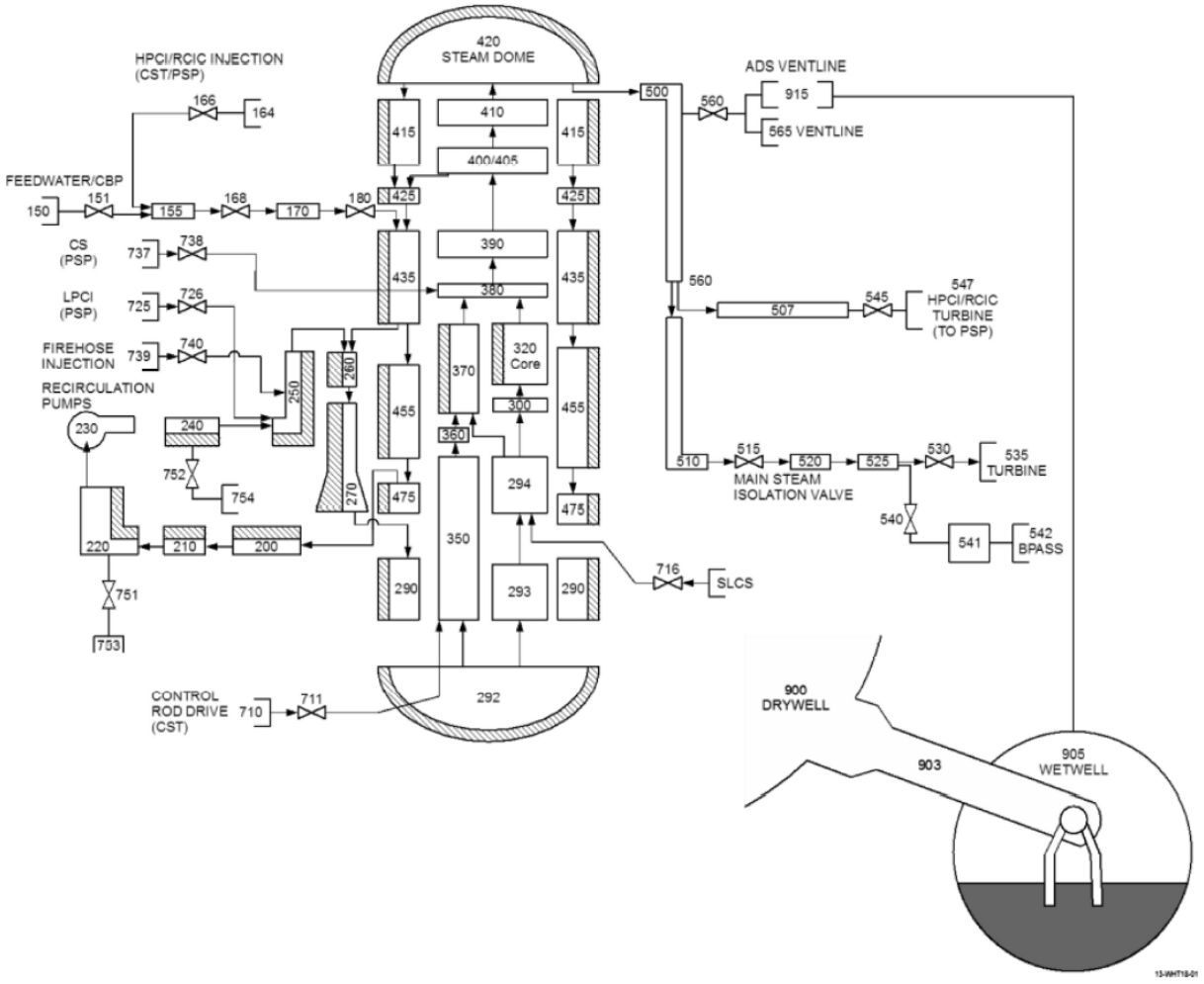

Figure 5-1. RELAP5-3D nodalization diagram

The safety systems mainly involve coolant injection into RPV to prevent fuel damage under BDBA conditions and they can be categorized into high pressure and low pressure safety systems. In a typical BWR-4 plant, high pressure safety systems include High Pressure Coolant Injection (HPCI), RCIC and Automatic Depressurization System (ADS). Low pressure safety systems include Low Pressure Coolant Injection (LPCI), low pressure CS, Firewater, standby liquid control system (SLCS), Control Rod Drive Hydraulic System (CRDHS).

The HPCI system works in a similar way as RCIC but it provides a greater water injection rate (about ten times greater than that of RCIC). It consists of a steam turbine-driven pump, valves and valve operators, and associated piping, including that from the normal and alternate pump suction sources and the pump discharge up

to the penetration of the main feedwater line. It is a single-train system actuated by either a low reactor water level or a high drywell pressure. Just like RCIC, HPCI initially operates in an open loop mode, taking suction from the CST. When the level in the CST reaches a low-level setpoint, the HPCI system is aligned to the SP. HPCI is an independent ECCS system that requires no auxiliary AC power to provide makeup water to the core under small to intermediate size LOCA accidents. The main difference between HPCI and RCIC is that the operation of HPCI will rapidly depressurize the RPV due to its large steam release rate, while the steam-driven turbines of HPCI rely on high pressure steam to operate.

There are thirteen SRVs connected on the steam exit pipe of the main steam line. SRVs can be manually controlled with DC power to limit the RPV pressure in a prescribed range or obtain the controlled depressurization of the reactor. Following a normal reactor shutdown, or reactor scram under accident scenarios, the decay heat continues to generate steam, albeit at a reduced rate. The turbine bypass system diverts the steam to the condenser if the RPV is not isolated from the secondary plant, or the steam will be vented to the SP through operation of the SRVs when the RPV is isolated. Among the 13 SRVs, 5 valves also serve in the ADS which can be employed to complete depressurizing the RPV in a short period of time. Once the RPV is completely depressurized by ADS, no core cooling is available unless AC power is recovered.

Low pressure ECCS systems such as LPSI and LPCS and firewater can be aligned to the RPV to inject coolant to the core when AC power is available and the RPV is depressurized. LPCI is the dominant mode of the RHR system. It takes water from the SP and discharges to the RPV to maintain the coolant inventory at a relatively low pressure. LPCS is capable of pumping water from the SP and spraying it on top of fuel assemblies.

The fuel design used in the core modeling is a representation of GE 8x8 fuel design. The fuel assembly geometry is an 8 x8 lattice. The basic fuel rod is comprised of a column of right circular cylinder fuel pellets enclosed by a cladding tube and sealed gas-tight by plugs inserted in each end of the cladding tube. The fuel pellets consist of sintered uranium-dioxide (UO2) or UO2-gadolinia solid solution ((U, Gd)O2) with a ground cylindrical surface, flat ends, and chamfered edges. Each full-length UO2 fuel rod may include natural enrichment UO2 pellets at each end of the fuel pellet column. The fuel rod cladding tune is comprised of Zircaloy-2 with a metallurgically bonded inner zirconium layer. Each fuel rod includes a plenum at the top of the fuel rod to accommodate the release of gaseous fission products from the fuel pellets. This gas plenum includes a compression spring to minimize fuel column movement during fuel assembly shipping and handling operations while permitting fuel column axial expansion during operation. Fuel rods are internally pressurized with helium to reduce the compressive hoop stress induced in the cladding tube by the coolant pressure and to improve the fuel to cladding heat transfer. With the absence of known data, the fuel rod’s internal pressure is assumed to be 1 MPa.

Table 5-2. Fuel parameters

Parameters	**Values**
Bundle assembly lattice	8x8
Number of full-length rods	62
Number of part length rods	0
Number of water rods	2
Active fuel length (cm)	381.0
Rod to rod pitch (cm)	1.295
Pellet Outer Radius (cm)	0.51694
Cladding Inner Radius (cm)	0.53980

Cladding Outer Radius (cm)	0.62615
Fuel channel thickness (cm)	0.2033

Since the reactor core has 764 fuel assemblies, and with 62 fuel rods within each assembly. The total number of fuel rods in the core is 47368, which renders tracking individual fuel rod impractical in systems transient analyses. Therefore, homogenization techniques would be used to lump fuel rods and flow channels into manageable numbers. Different homogenization approaches are used for thermal fluid dynamics calculations for the two-phase flow in the fuel assemblies than for the heat conduction and clad oxidation calculations in the fuel rods. For the thermal fluid dynamics calculations, one flow channel is built to simulate the active flow within the 764 fuel assemblies. The flow channel (average channel) represents the active flow in all the assemblies of the core.

For heat conduction and clad oxidation calculations, one set of heat structures is built to represent the average of all the fuel rods in the 764 fuel assemblies.

These homogenization approaches are reasonable as they greatly speedup the simulation time, and capture the flow behaviors in the flow channels as well as the temperature profiles and oxidation behaviors in the fuel rods. As a result, the heat structures for all the fuel rods in the 764 assemblies are lumped into one set and are attached to the flow in the average channel, as shown in Figure 5-2.

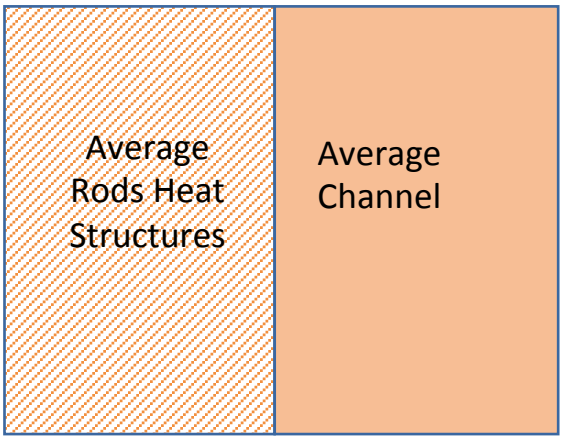

Figure 5-2. Schematic illustration of the heat structure mapping for all the assemblies and their respective fuel rods with the average flow channel.

The neutron energy spectrum can vary during an operation cycle to generate and utilize more plutonium from the non-fissile U-238 by changing the void fraction in the core through control of the core coolant flow rate. This operation method, which is called a spectral shift operation, is practiced in BWRs to save natural uranium. The core power shapes, as a function of cycle burnup state, have significant impact on the temperature distributions in the core. For a typical BWR core, the power shapes tend to be bottom peaked near the beginning-of-the-cycle (BOC). As the cycle depletion progresses, the power shapes gradually evolve into cosine shape near the middle-of-the-cycle (MOC). Toward the end-of-the-cycle, the power shapes tend to be top peaked. For simplicity, in this analysis, the bottom peaked power shapes are used in the transient calculations.

5.2 Demonstration of RCIC "Self-Regulating" Operations Under SBO Conditions

In the station blackout scenario [14, 15], it is hypothesized the loss of all off-site and on-site AC power (emergency diesel generators fail to start or run) happens following initiating events such as internal fire, flood or seismic events. The reactor, however, is successfully scrammed immediately following initiating events. The main steam line isolation (MSIV) valves are closed and the main feedwater pumps cease operating so the reactor core becomes isolated. The turbines are tripped and turbine bypass valves remain closed so the containment becomes isolated. The LPCI, CS, firehose injection, SLCS and CRDHS are not available due to the loss of AC power. SRVs are available because the valves can be opened and closed by passive forces. It is further assumed that the on-site direct current (DC) power is not available immediately following the initiation of SBO such that the RCIC operation will not be properly controlled and will enter "self-regulating" mode of operations.

The SBO simulation was performed for 24 hours following the initiation of SBO. The RCIC self-regulating mode of operations is clearly demonstrated with the simulation. Figure 5-3 shows the RCIC pump water mass flow rate without any controls. It can be seen that the water mass flow rate into the RPV oscillating around 20 Kg/s for the first 6 hours when the Terry turbine nozzle inlet condition is pure steam as shown by the nozzle inlet void fraction in Figure 5-4. As the transient progresses past 6 hours, the nozzle inlet starts to experience two-phase flow conditions which indicate that the main steam line experiences flooding and the RCIC pump water mass flow oscillates around 12.5Kg/s for the remainder of the SBO transient. The self-regulated RCIC water injection is able to keep the fuel covered as shown in Figure 5-5 for the collapsed water level in the flow channel. Figure 5-6 shows the collapsed water level in the RPV downcomer. Figure 5-7 shows the RPV dome pressure during the SBO. Figure 5-8 shows the steam mass flow rate through the Terry turbine nozzles during the SBO. During the first 6 hours, the steam mass flow rate is higher when the nozzle inlet condition is pure steam and the steam mass flow rate is oscillating at a lower rate beyond 6 hours with a two-phase flow condition at the nozzle inlet. Figure 5-9 shows the water mass flow rate through the nozzle during the SBO.

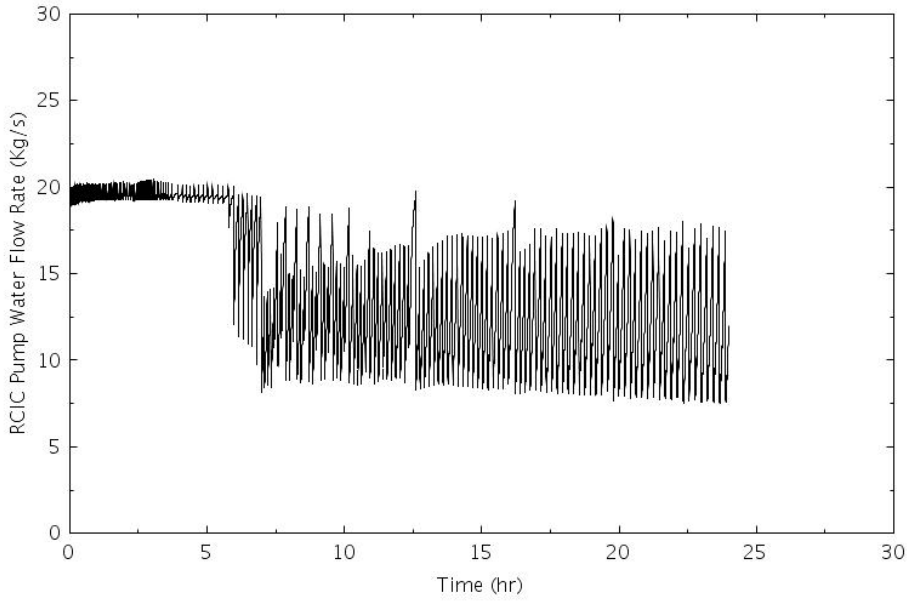

Figure 5-3. RCIC pump water flow rate during SBO

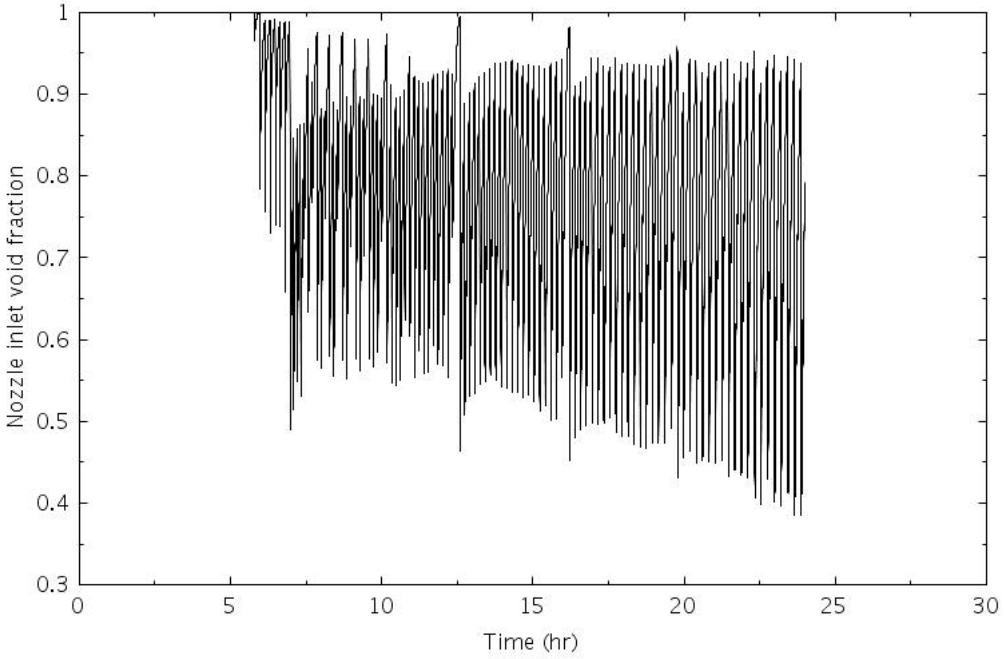

Figure 5-4. Terry turbine nozzle inlet void fraction

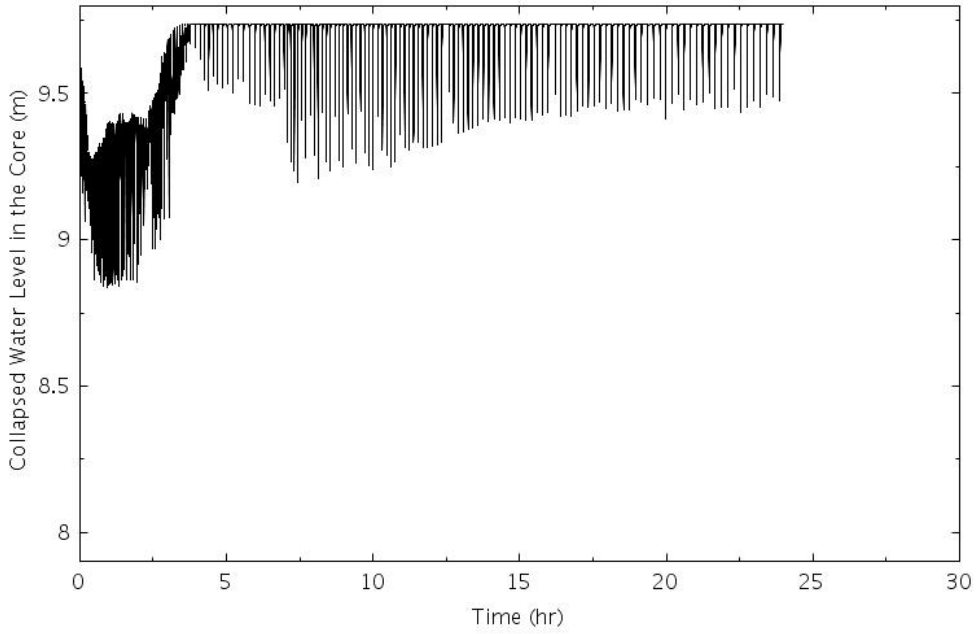

Figure 5-5. Flow channel collapsed water level during SBO

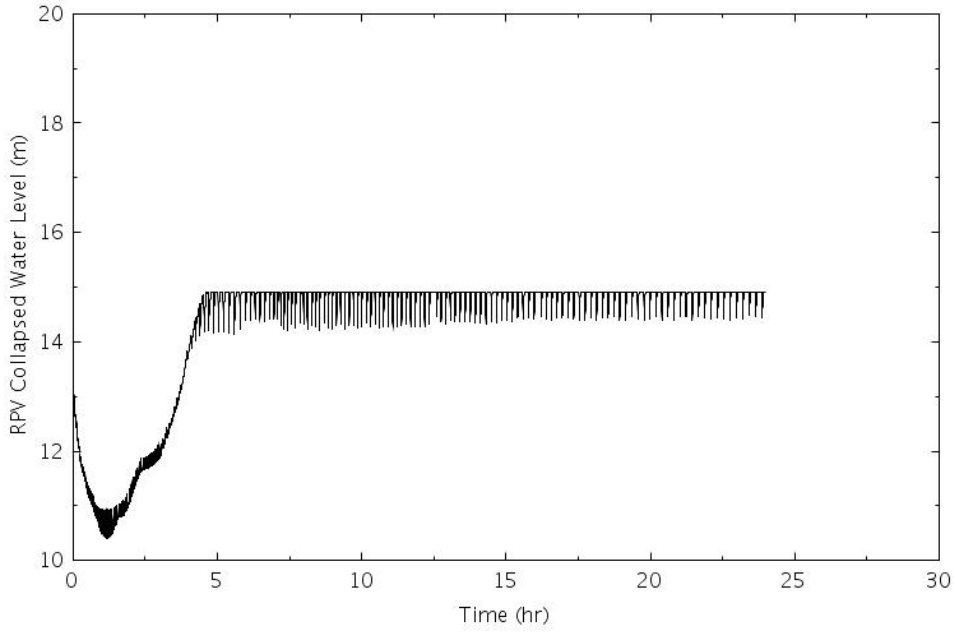

Figure 5-6. RPV collapsed water level during SBO

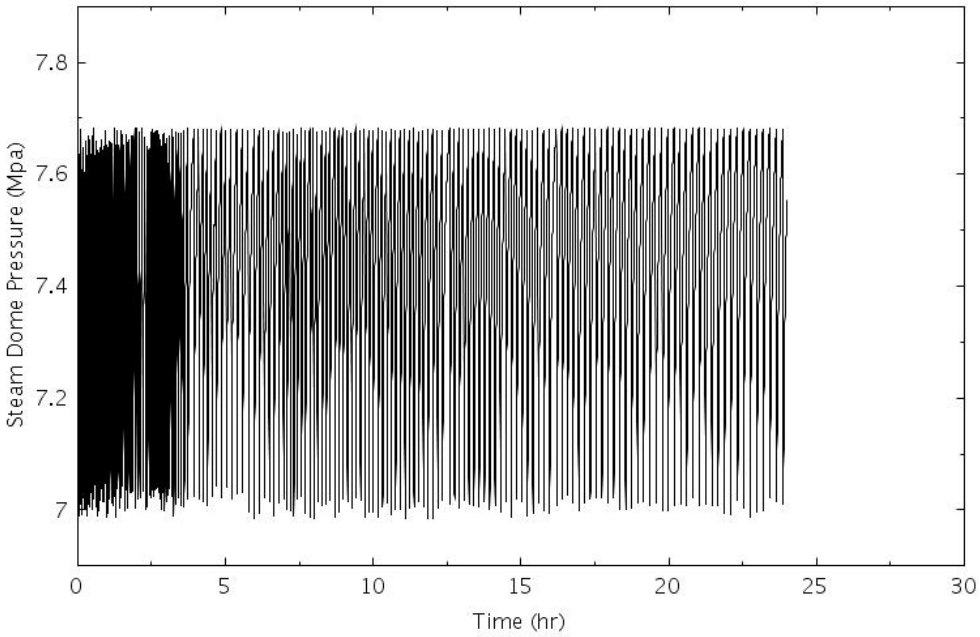

Figure 5-7. RPV dome pressure during SBO

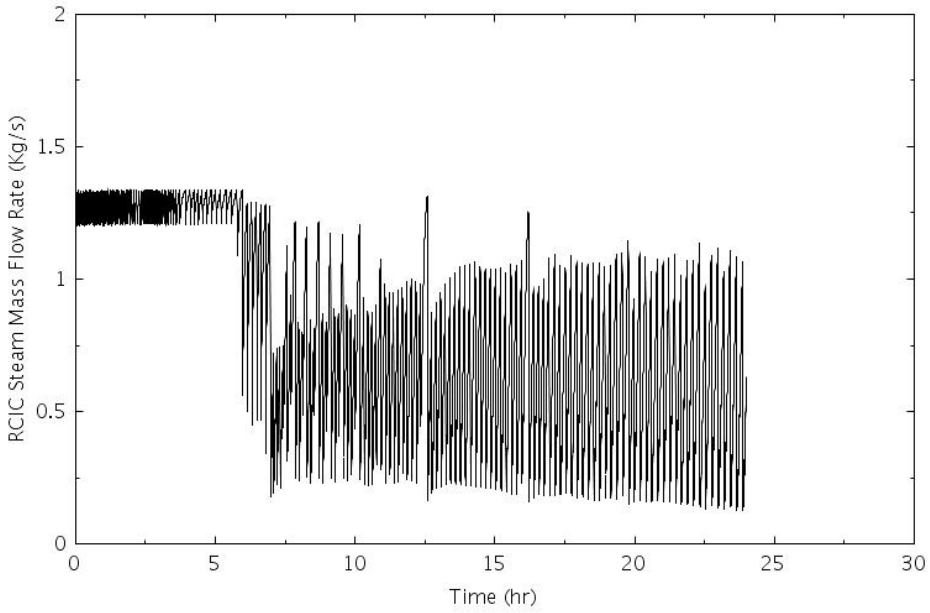

Figure 5-8. Nozzle steam mass flow rate during SBO

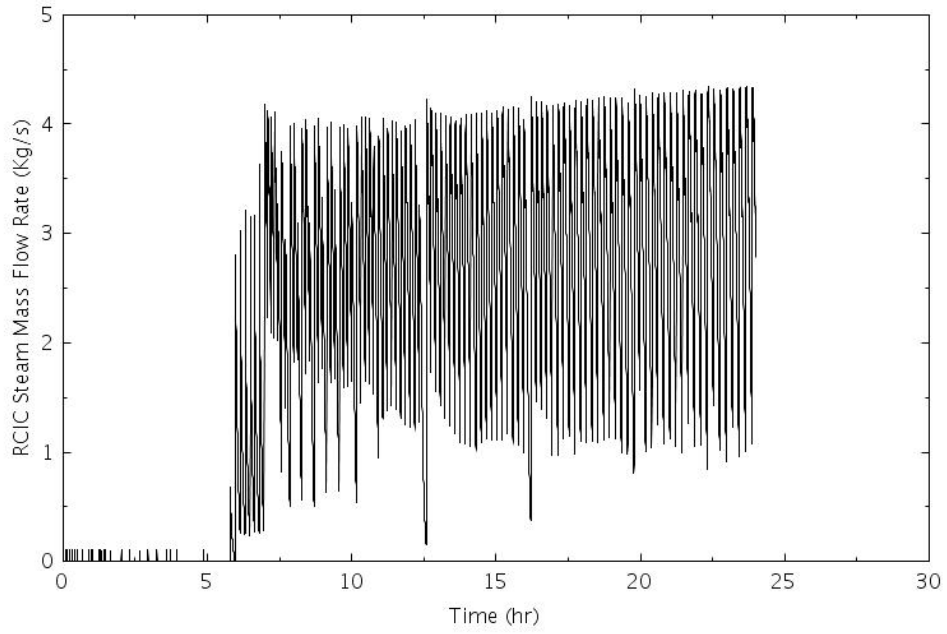

Figure 5-9. Nozzle water flow rate during SBO

6. CONCLUSIONS

This report documents the FY 2020 activities on developing improved models for Terry turbine nozzles and the implementation of the models into the RELAP5-3D code. To present a complete picture of the model development, the previously developed three models – Mach area relations, the isentropic homogenous equilibrium model (IHEM), and the Moody critical flow model – are summarized in section 2. The Mach area relations and the IHEM work better under pure vapor conditions at the Terry turbine nozzle inlet. For mixed inlet conditions, the Moody critical flow model provides a means of providing an upper bound for the choked mass flow at the throat, but is less accurate on predicting phasic velocities at the nozzle exit. With the motivation to develop a fast-running model that can be implemented into a reactor system analysis code like RELAP5-3D and to address the full range of possible two-phase and single-phase inlet conditions at Terry turbine nozzles, a HMDEM is developed in this work. Section 3 presents the detailed development of the HMDEV. Section 4 presents the model implementation into the RELAP5-3D code, model verification and partial validation. A polynomial representation of the HMDEM is performed, allowing for a lower order implementation into RELAP5-3D. This effort, in turn, allows the RELAP5-3D code to have the capability to mechanistically model the Terry turbine behavior during the complex, multiphase processes which occur during a SBO in a BWR. The validation reveals a strong agreement with the historical Knease nozzle experiment, a data set which had been partially elusive to capture in past modeling efforts.

Section 5 presents the simulation results of a station blackout (SBO) scenario for a generic BWR plant model using RELAP5-3D with HMDEM implemented for the simulation Terry turbine nozzles as well as analytical models for the Terry turbine rotor. The simulation results clearly demonstrated the “self-regulating” mode of operation of RCIC during SBO without any controls. The demonstrated capability of RCIC to operate in a self-regulated mode without external controls provides much longer coping time for FLEX to be installed to mitigate an SBO accident. Hence the self-regulation operation of RCIC allows its operation band and flexibility to be expanded and provide enhanced safety margins to the plant.

With further validation of the model, HMDEM has the potential to provide the results needed to credit the RCIC self-regulation operations in accident management and mitigation.

7. REFERENCES

1. K. ROSS, et. al., *Modeling of the Reactor Core Isolation Cooling Response to Beyond Design Basis Operations – Phase 1*, SAND2015-10662, December, (2015).
2. https://www.nrc.gov/docs/ML1209/ML120970422.pdf.
3. R. GAUNTT, et. al., *Fukushima Daiichi Accident Study*, SAND2012-6173, Sandia National Laboratories, Albuquerque, NM, August (2012).
4. RELAP5-3D© Code Manual Volume I: Code Structure, System Models and Solution Methods, INL/MIS-15-36723 Revision 4.3 October 2015.
5. Haihua Zhao, Hongbin Zhang, Ling Zou, James O'Brien, "Single Phase Analytical Models for Terry Turbine Nozzle," *Proceedings of ICAPP'17*, April (2017).
6. H. Zhao and J. O'Brein, "A Two-Phase Analytical Model for Terry Turbine Nozzle," *Transactions of the American Nuclear Society*, **Vol. 117, (**2017).
7. H. Zhang and L. Zou, "Development of Analytical Models for RCIC Terry Turbine and Pump", *International Topical Meeting on Advances in Thermal Hydraulics (ATH'18)*, Orlando FL, November 11-15, 2018.
8. Strickland L. Kneass (1910), "Practice and Theory of the Injector".
9. Wenwen Zhanga, Dean Wanga, Ananthi Renganathana, and Hongbin Zhang (2020), " Modeling and assessment of two-phase transonic steam flow with condensation through the convergent-divergent nozzle", *Nuclear Engineering and Design*, Vol. 364.
10. John D Anderson (2003), "Modern Compressible Flow with Historical Perspective" Third Edition, McGraw-Hill Series in Aeronautical and Aerospace Engineering.
11. Cole Blakley and Hongbin Zhang, "Improved Compressible Two Phase Analytical Model for Steam Nozzle Application", to be submitted to *Nuclear Engineering and Design*.
12. Juan José Gómez Romera, http://www.iapws.org/release.html, 2018.
13. Han Bao, Jinyong Feng, Nam Dinh, Hongbin Zhang, "Computationally efficient CFD prediction of bubbly flow using physics-guided deep learning", International Journal of Multiphase Flow, Volume 131, October 2020, 103378.
14. State-of-the-Art Reactor Consequence Analyses Project Volume 1: Peach Bottom Integrated Analysis, NUREG/CR-7110, Vol. 1, 2012.
15. Xu Wu and Koroush Shirvan, "System code evaluation of near-term accident tolerant claddings during boiling water reactor short-term and long-term station blackout accidents", *Nuclear Engineering and Design*, https://doi.org/10.1016/j.nucengdes.2019.110362.